

Electrophoretic deposition of novel semi-permeable coatings on 3D-printed Ti-Nb alloy meshes for guided alveolar bone regeneration

Zhao, Danlei; Dong, Haoran; Niu, Yuting; Fan, Wenjie; Jiang, Muqi; Wei, Qingsong; Palin, Will; Zhang, Zhen; Li, Ke

DOI:

[10.1016/j.dental.2021.12.026](https://doi.org/10.1016/j.dental.2021.12.026)

License:

Creative Commons: Attribution-NonCommercial-NoDerivs (CC BY-NC-ND)

Document Version

Peer reviewed version

Citation for published version (Harvard):

Zhao, D, Dong, H, Niu, Y, Fan, W, Jiang, M, Wei, Q, Palin, W, Zhang, Z & Li, K 2021, 'Electrophoretic deposition of novel semi-permeable coatings on 3D-printed Ti-Nb alloy meshes for guided alveolar bone regeneration', *Dental Materials*. <https://doi.org/10.1016/j.dental.2021.12.026>

[Link to publication on Research at Birmingham portal](#)

General rights

Unless a licence is specified above, all rights (including copyright and moral rights) in this document are retained by the authors and/or the copyright holders. The express permission of the copyright holder must be obtained for any use of this material other than for purposes permitted by law.

- Users may freely distribute the URL that is used to identify this publication.
- Users may download and/or print one copy of the publication from the University of Birmingham research portal for the purpose of private study or non-commercial research.
- User may use extracts from the document in line with the concept of 'fair dealing' under the Copyright, Designs and Patents Act 1988 (?)
- Users may not further distribute the material nor use it for the purposes of commercial gain.

Where a licence is displayed above, please note the terms and conditions of the licence govern your use of this document.

When citing, please reference the published version.

Take down policy

While the University of Birmingham exercises care and attention in making items available there are rare occasions when an item has been uploaded in error or has been deemed to be commercially or otherwise sensitive.

If you believe that this is the case for this document, please contact UBIRA@lists.bham.ac.uk providing details and we will remove access to the work immediately and investigate.

Electrophoretic deposition of novel semi-permeable coatings on 3D-printed Ti-Nb alloy meshes for guided alveolar bone regeneration

Danlei Zhao^{abcd1}, Haoran Dong^{abc1}, Yuting Niu^{abc}, Wenjie Fan^{abc}, Muqi Jiang^{abc}, Ke Li^{abc}, Qingsong Wei^d, William M.Palin^e, Zhen Zhang^{abce}

^aDepartment of Stomatology, Union Hospital, Tongji Medical College, Huazhong University of Science and Technology, Wuhan 430022, China

^bSchool of Stomatology, Tongji Medical College, Huazhong University of Science and Technology, Wuhan 430030, China

^cHubei Province Key Laboratory of Oral and Maxillofacial Development and Regeneration, Wuhan 430022, China

^dState Key Lab of Materials Processing and Die & Mould Technology, School of Materials, Science and Engineering, Huazhong University of Science and Technology, Wuhan 430074, China

^eDental and Biomaterials Sciences, School of Dentistry, Institute of Clinical Sciences, College of Medical and Dental Sciences, University of Birmingham, UK

Abstract

Objective

Guided bone regeneration (GBR) techniques use barrier membranes to augment the alveolar ridge for the site-specific growth of bone defects. However, current approaches using cast metal substructures exhibit poor adaptation to the surgical site and increased risk of infection. This study aimed to fabricate multifunctional coatings with 3D-printed porous titanium-niobium (Ti-Nb) alloy meshes to maintain space, prevent the ingrowth of fibroblasts and inhibit the colonization of bacteria for GBR.

Methods

Ti-Nb alloy meshes were prepared by selective laser melting (SLM) and used as substrates for novel surface coatings. Porous chitosan (CS)/ gelatin (G)/ doxycycline (Dox) coatings were formed on the meshes using electrophoretic deposition (EPD) and freeze-drying. The process of EPD was characterized through Fourier transform infrared spectroscopy (FT-IR), zeta potential, and particle size analysis. The cytotoxicity of the coatings was evaluated through the culture of osteoblasts and immunostaining. The antibacterial activity of the coatings was tested using inhibition zone tests against *Staphylococcus aureus* (*S. aureus*) and scanning electron microscope (SEM). The inhibition of fibroblasts infiltration and nutrients transfer properties were analyzed using immunostaining and permeability tests.

Results

High yield strength (567.5 ± 3.5 MPa) and low elastic modulus (65.5 ± 0.2 GPa) were achieved in Ti-Nb alloy bulk samples. The data of zeta potential, FT-IR and SEM indicated that porous spongy coatings were chemically bonded following EPD. *In vitro* analysis of CSGDox1 (containing Dox at $1 \text{ mg} \cdot \text{mL}^{-1}$) coating revealed its antibacterial effect and biocompatibility. Moreover, the CSGDox1 coating was proved to be effective for preventing the ingrowth of fibroblasts, whilst allowing the infiltration of nutrients.

Significance

This study verified that the EPD of CSGDox coatings on the 3D-printed Ti-Nb membrane can maintain space, provide antibiotic release whilst maintaining a barrier against soft-tissue growth, which is essential for the success of GBR treatment.

Keywords: Guided bone regeneration, 3D-printing, Electrophoretic deposition, Chitosan, Gelatin, doxycycline.

1. Introduction

Alveolar bone defects can be induced by serious infection including periodontitis, periimplantitis and radicular cysts, or other factors such as physiologic atrophy, trauma, tumor incision and ectodermal dysplasia [1]. Reconstruction of the alveolar bone is a key prerequisite for rebuilding the masticatory and aesthetic function of teeth. Autogenous bone grafts have been considered the gold standard for alveolar bone augmentation. However, there exist significant contraindications for their use, including the limited quantity of autogenous supply and donor site injury. Consequently, a multidisciplinary approach involving materials and biomedical scientists, chemists and clinicians is required to develop alternative biomaterials that will reduce or eliminate the need for autografts [2].

Guided bone regeneration (GBR) utilizes bone graft or osteoinduction materials for bone reconstruction and stability of blood clot formation [3]. The PASS principle, including Primary wound closure, Angiogenesis, Space maintenance, and Stability of both the initial blood clot and implant fixture, is recognized as the four major factors underlying successful GBR [4]. Moreover, the membrane used for GBR is an indispensable part of the treatment, which can be classified as bioabsorbable or non-resorbable materials (polymers, metals and compounds). Due to the high turnover rate of soft tissues, membranes are used to separate the graft from soft tissues. This approach prevents soft tissues from occupying the space of bone formation. An ideal membrane, especially for large defects, would effectively screen the rapidly proliferating epithelium while providing enough structural support for osteogenesis during the surgery and throughout healing.

Titanium meshes with excellent mechanical properties are now widely used as barrier membranes to provide space for bone graft materials in GBR procedures [5]. However, current titanium meshes still exhibit major drawbacks related to poor clinical manageability. The limited material conformability for adaptation to the bone defect surface during surgery and the sharp edges produced by contouring increases the likelihood of membrane exposure [6]. Previous research has explored additive manufacturing of titanium alloy by selective laser melting (SLM) to produce near-net-shape mesh structures [7, 8]. The shape of the 3D-printed titanium mesh could be customized to match that of the bone defect area. Moreover, porous structures are capable to be realized in the meshes through SLM for further function design.

In addition to the requirement for space, the capacity to inhibit fibroblast infiltration and allow nutrient transfer is also a key requisite for membranes. The combination of coatings and 3D-printed titanium meshes can simultaneously achieve structural support and multi-function. Among coating strategies, electrophoretic deposition (EPD), as a liquid-based method, can be applied to fabricate a coating on porous titanium meshes [9]. Chitosan (CS) is a natural cationic polymer that is widely used in the biomedical field due to its biocompatibility and biodegradability [10]. Gelatin (G) is a natural macromolecular material derived from collagen and has been widely used as food ingredients and pharmaceutical capsules [11]. In EPD, charged chitosan and gelatin composite colloidal particles suspended in an aqueous solution are attracted and deposited onto a titanium substrate under an electric field [12, 13]. The formation of sponge-like structures could be used to control the permeability of meshes to realize the protein transfer and the exclusion of epithelial and connective tissues.

The achievements of GBR have often been compromised by bacterial colonization and infection, mainly when the barrier membranes were exposed. Antibiotics are often used for days following a GBR procedure to prevent potential infection [14]. However, the application of systemic antibiotics often fails to form an effective concentration around the bone graft due to their relatively poor penetrability. Conversely, locally applied antibiotics can release high concentrations from the membrane surface *in situ*, effectively preventing infection and avoiding the drawbacks of their systemic application [15, 16]. Doxycycline (Dox), a widely-used antibiotic, shows inhibitory effects on inflammation and osteoclast genesis with the capacity to stimulate bone formation [17-19]. Therefore, Dox was loaded on CS/G coatings for the prevention of bacterial infection.

In this work, SLM-printed Ti-Nb alloy meshes were chosen as substrates for surface coatings. Porous CS/G/Dox coatings were deposited on the mesh through electrophoretic deposition and freeze-drying. Fourier transform infrared spectroscopy (FT-IR), zeta potential, and particle size analysis were used to study the EPD process. The coatings achieved favorable biocompatibility and antibacterial activity. Moreover, it demonstrated the capacity to inhibit the fibroblasts' infiltration, accompanying with nutrients transfer *in vitro*. The results suggest that the multi-functional membrane possesses the clinical translational capability to treat alveolar bone defects.

2. Materials and Methods

2.1 Specimen preparation

The fabrication process and mesh design are depicted in Fig. 1. SLM was used to print Ti-Nb alloy meshes on a pure titanium substrate within a high purity argon (99.9%) inert environment. Based on an optimization procedure, the process parameters were used as: a laser power of 320 W, a scanning speed of 800 mm/s, a hatching space of 100 μm , and a powder layer thickness of 30 μm . A gas atomized spherical pure Ti powder (AMC Powder, China) and a mechanically crushed Nb powder (Puwei, China) with mean particle sizes of 27.1 μm and 8.66 μm , respectively, were used as precursor materials (Fig. 1b).

An optimal mass ratio Ti and Nb was set as of 60:40 according to previous investigations [20]. Bar-shaped specimens ($10 \times 10 \times 6 \text{ mm}^3$ and $65 \times 10 \times 2 \text{ mm}^3$) were printed for analysis of microstructure and tensile properties, respectively. Biological test specimens (14 mm diameter, 0.5 mm thickness) were also prepared. Three types of lattice with 1000 μm cell size patterns (Tetragon, T1000; Hexagon, H1000; Round, R1000; Fig. 1c) were adopted for the metal mesh design (Unigraphics NX8.0 software).

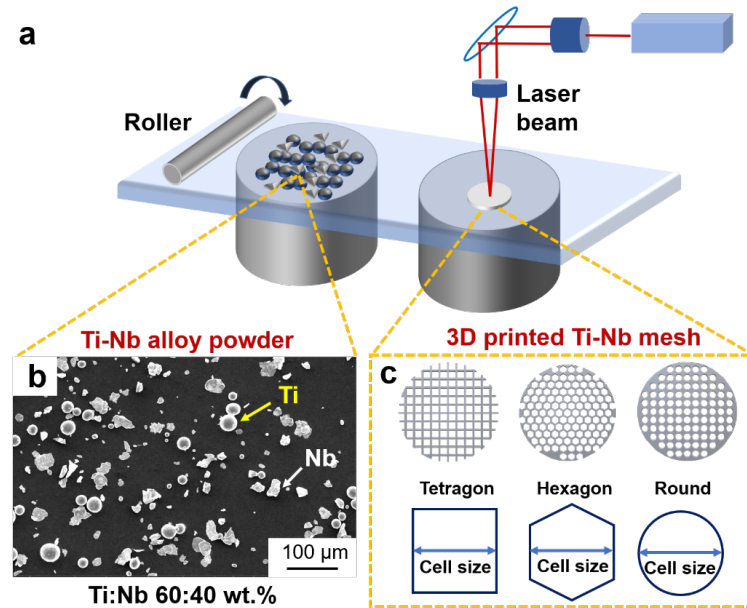


Fig. 1. Additive manufacturing of Ti-Nb alloy meshes. **(a)** Schematic illustration of the SLM process; **(b)** SEM images showing the Ti-Nb powders and **(c)** Mesh design files and the definition of cell size.

2.2 Microstructural and mechanical characterization

The morphologies and microstructure of the printed Ti-Nb alloy were observed by a

scanning electron microscope (SEM, JSM-7600F), equipped with energy disperse spectrometer (EDS). The specimens were surface ground, polished and etched with a solution consisting of HNO₃ (3 mL), HCl (6 mL) and H₂O (92 mL) for 30 s. The grain map, grain boundaries and phase composition of the printed Ti-Nb alloy were identified using electron backscatter diffraction (EBSD, Oxford) and an X-ray powder diffractometer (XRD, PANalytical, Netherlands), respectively.

Nanoindentation was carried out on the Ti-Nb alloy meshes using a high-precision nano-hardness scratch tester (TI750, Hysitron, American) with a load of 3500 mN and an indentation time of 2 s to calculate surface hardness and elastic modulus (n=3). The tensile properties of the Ti-Nb alloy were determined using a universal testing machine (MTS Bionix, USA) with a strain rate of 0.5 mm min⁻¹. Fractography was characterized using the SEM in the secondary electron (SE) mode.

2.3 Surface coating preparation

Chitosan (Golden-Shell Biochemical, China; 1,000,000 Mw, 7.86% humidity, 0.80% ash content, >95% deacetylation degree), Doxycycline (D111943, Aladdin Industrial Corporation, China) and gelatin (type A, V900863, Sigma, USA) were used. Chitosan solution (10 mg·mL⁻¹) was prepared by dissolving chitosan in 0.06M HCl solution and stirring for 24 h at room temperature. CSG solution (10 mg·mL⁻¹) was prepared by dissolving gelatin powder in chitosan solution and stirring for 2 h at 60 °C. CSGDox composite solutions containing Dox at 1 mg·mL⁻¹ (CSGDox1) and 10 mg·mL⁻¹ (CSGDox10) concentration was prepared separately.

Ti-Nb meshes were used as the cathode and a parallel platinum plate as the anode. Both cathode and anode were immersed in CSG or CSGDox solution with a fixed distance of 6 cm. A constant electric voltage of 15 V for 1 minute was applied by a direct current power supply (Model 6614C, Agilent Technologies, USA).

Upon EPD, the samples were disconnected from the power supply, removed from the solution, enwrapped in aluminum foil to protect from ambient light, and stored in a refrigerator at -18°C. The coatings were then prepared by lyophilizing samples (Biosafer-10D) for a further 24 h, and stored in a drying box, also enwrapped in aluminum foil for further experiments.

2.4 Characterization of deposited coatings

Measurements of zeta potential and particle size of the electrolyte solutions and colloids were performed by photon correlation spectroscopy (Zetasizer 3000 Malvern Instruments, U.K; n=3). The functional groups of the coatings were identified by ATR-FTIR (Nicollet 5700, Thermo, USA; n=3) at room temperature ($21 \pm 1^\circ\text{C}$).

2.5 Antibacterial Efficacy

Staphylococcus aureus (American Type Culture Collection, 25923) was cultured in Mueller-Hinton Broth (MHB). The bacterial suspension (1 mL of 10^8 cfu mL^{-1} , calculated using spread plate count) was applied uniformly on the surface of a nutrient agar plate, after which coated titanium substrates were placed on the plates and incubated at 37°C for 24 h. The inhibition zone around the samples (if any) was subsequently measured once a day for 7 days. For adhesion experiments, the bacterial concentration was further adjusted to $1 \times 10^6\text{ cfu mL}^{-1}$ in PBS. The samples were immersed in 4 mL of the suspension and inoculated at 37°C for 12 h with shaking. After thorough washing with PBS, the samples were dehydrated through a series of graded ethanol concentrations and the surface gold coated for subsequent SEM observation.

2.6 Cell culture

Primary human dermal fibroblasts were isolated from human prepuce tissue, kindly provided by the Urinary Surgery Department of Union Hospital. Fibroblasts and MC3T3 osteoblast-like cells were cultured in Dulbecco's Modified Eagle's Medium (DMEM; Gibco Lab., Grand Island, NY, USA) supplemented with 10% fetal bovine serum (FBS; Gibco, USA) at 37°C in a humidified 5% CO_2 atmosphere. The culture medium was refreshed every 2 days. When cells reached 80-90% confluence, they were trypsinized, centrifuged and suspended in the culture medium. The 3 samples of coated titanium substrates were steam sterilized (121.3°C , 30 min) and then placed in 24-well tissue culture plates under aseptic conditions with 1 mL of medium. They were seeded at a density of 40000 cells per well.

2.7 Cell skeleton

After 3 days of culture, the samples were washed with PBS and then fixed with paraformaldehyde for cell skeleton observation. After being washed with PBS, samples

were permeabilized with 0.1% Triton X-100 solution for 5 min. The nonspecific binding sites were blocked by incubating the coatings in PBS containing 1% bovine serum albumin for 30 min. Filamentous actins (F-actins) were stained with rhodamine phalloidin (R-415 kit, Molecular Probes, Invitrogen, USA) for 20 min at room temperature. The nuclei were stained with 2-(4-amidinophenyl)-6-indolecarbamide dihydrochloride (DAPI; 1:1000 dilutions in PBS; Invitrogen, Basel, Switzerland) for 15 min at room temperature. The samples were rinsed again with PBS and then stored in 9:1 glycerol/PBS. Immunofluorescence images were obtained using a Nikon TE-2000 inverted microscope.

2.8 Inhibition of fibroblast infiltration

This experiment was done by using a self-made *in vitro* model (Fig. 2). Firstly, a steam-sterilized hollow stainless-steel cylinder (external diameter 14 mm, height 8 mm) was placed in a 24-well plate. 1 mL of DMEM medium was added to the well in advance, then CSGDox1 coated porous Ti-Nb meshes (14 mm diameter) were placed on, and completely covered the cylinder. Further, 0.5 mL of cell culture medium containing 40000 cells per well was added to the upper surface of each porous Ti-Nb alloy mesh. After 72 h of culture, the media was removed. The cells were then rinsed with PBS, fixed with fluorescence staining and graded dehydration, and observed by fluorescence microscopy and SEM.

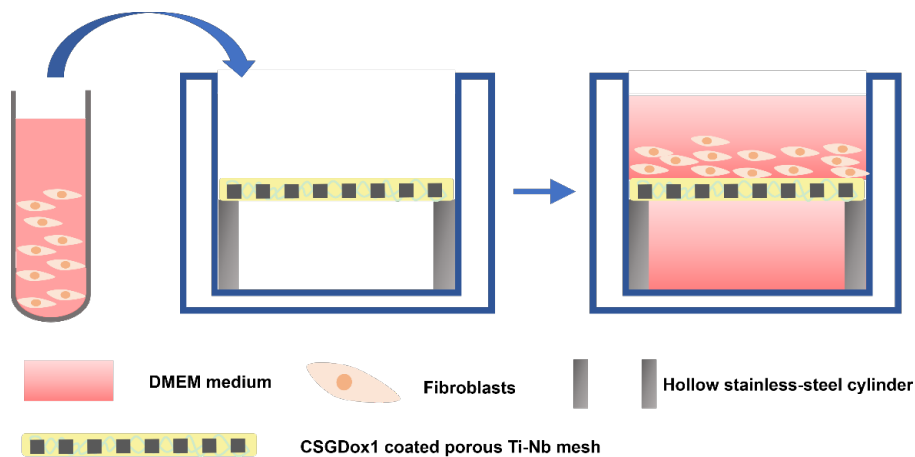


Fig. 2. A schematic diagram of the experimental model of the inhibition of fibroblast infiltration tests.

2.9 Diffusion of protein

The membrane pores should also facilitate the diffusion of fluids and proteins, which

are vital for bone regeneration, such as growth factors and bioactive substances for cell growth. Dental wax sheets (base plate wax, Shanghai Dental Materials Factory Changshu Branch, China) were used to wrap and seal the three groups of Ti-Nb alloy meshes (T1000, H1000, R1000, 6 samples for each group) to form the columnar permeation models, and then placed directly above the 24-well plate (Fig. 3). 1 mL of bovine serum albumin (BSA) solution (70 mg/mL) was added to the columnar models separately (cross-sectional area = $1.54 \times 10^{-4} \text{ m}^2$). The effective permeability of protein could be calculated by

$$EP(\text{protein}) = \frac{V(\text{protein})}{S \cdot t} \quad (1)$$

Where EP is the effective permeation [$\text{mL}/(\text{m}^2 \cdot \text{s})$], V is the volume of BSA solution [mL], S is the cross-sectional areas of the columnar model [m^2] and t is the processing time (s).

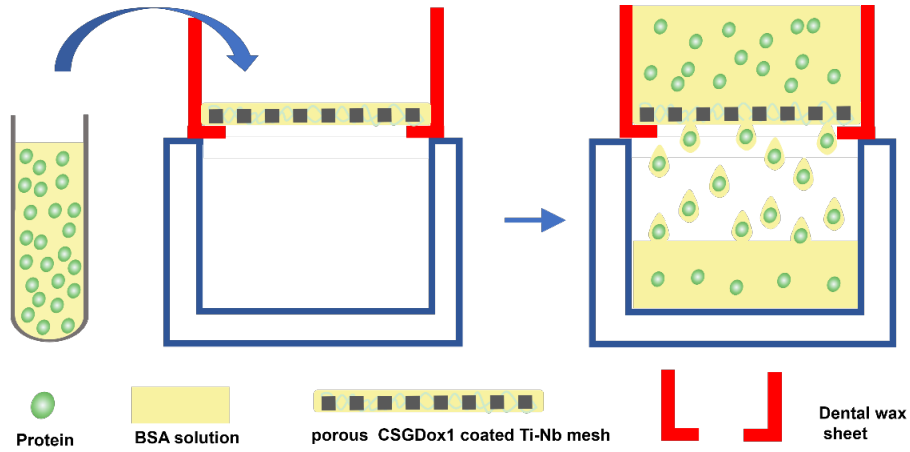


Fig. 3. A schematic diagram showing the experimental model of the diffusion of protein tests.

2.10 Statistical analysis

Statistical analysis was performed using SPSS v.25.0, and data were presented as mean \pm standard deviation (SD). Student's t test was used to determine statistical significance, with the level of significance set as ($P < 0.05$).

3. Results

3.1 Material characterization

Fig. 4a-c show the surface morphologies and strut geometries of T1000, H1000 and R1000 3D-printed Ti-Nb alloy meshes. The struts of meshes were fully interconnected

without observable damage and interlayer delamination, which was comparable to the designed files. Fig. 4d-g show the microstructural characteristics and the elemental distribution of the Ti-Nb alloy in the meshes. Cellular dendritic grains from the top view (Fig. 4d) and fine columnar grains from the lateral view (Fig. 4e) could be observed in the printed sample. The cellular grain which was oriented in different directions indicated that the metastable β -phase of Ti was retained. The Nb element lowered the β transition temperature, thereby retaining more β phase. The obtained β phase contributed to a decrease in elastic modulus (Fig. 4b), which may help to reduce the deleterious effects of stress-shielding. Fig. 4f suggested that the Nb element was homogenously distributed in the center and the side of the melt pool.

The grain maps identified by EBSD (Fig. 4g, top view) further highlighted the grain morphology and dimensions. The results indicated that the Ti-Nb alloy was entirely composed of large β -phase grains and no acicular shapes associated with α -phase were observed. Fig. 4h displays the grain boundary map of the Ti-Nb alloy. The dominated high-angle grain boundaries (HAGBs, $>15^\circ$) in the Ti-Nb alloy suggested favorable plasticity. The phase composition of the blended powder and the as-built meshes were identified (Fig. 4i). The XRD results further verified that Nb was capable to enhance the formation of β -phase during the printing process. In comparison with the XRD result of raw materials, no α -phase could be detected in the spectra of Ti-Nb alloy.

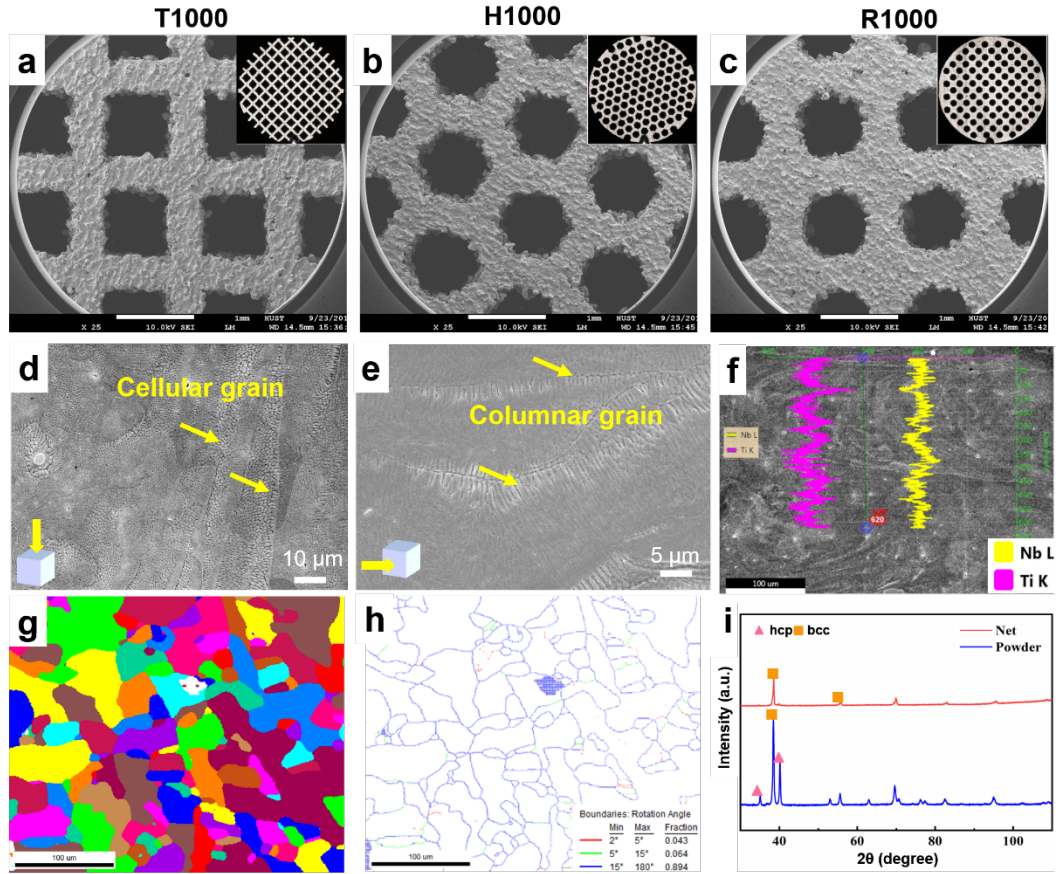


Fig. 4. Morphologies and microstructural observation of the Ti-Nb alloy meshes. (a-c) SEM images showing the surface morphologies of T1000, H1000 and R1000 meshes, respectively; (d-e) Microstructure of the mesh form top view and lateral view; (f) EDS line scanning of the melt pool in the top plane of the mesh and corresponding results; (g) Grain maps (a colour represents one grain); (h) Grain boundary maps and (i) XRD results.

3.2 Mechanical properties

Fig. 5a depicts the calculated nano-hardness and elastic modulus of the printed samples by nano-indentation (2.71 ± 0.3 GPa and 58.8 ± 1.5 GPa, respectively). Fig. 5b displays the tensile stress-strain response of Ti-Nb alloy. The printed alloy possessed an ultimate tensile strength of 735.4 ± 1.3 MPa, yield strength of 567.5 ± 3.5 MPa, the elastic modulus of 65.5 ± 0.2 GPa and elongation of $9.17 \pm 0.5\%$. In comparison with Ti6Al4V, Ti-Nb alloy possessed lower modulus and higher elongation, demonstrating the potential for dental applications [21]. Fig. 5c-d display the representative fracture surface of Ti-Nb alloy after tensile tests. The fine dimples were indicative of ductile fracture in the Ti-Nb alloy and consistent with increased ductility.

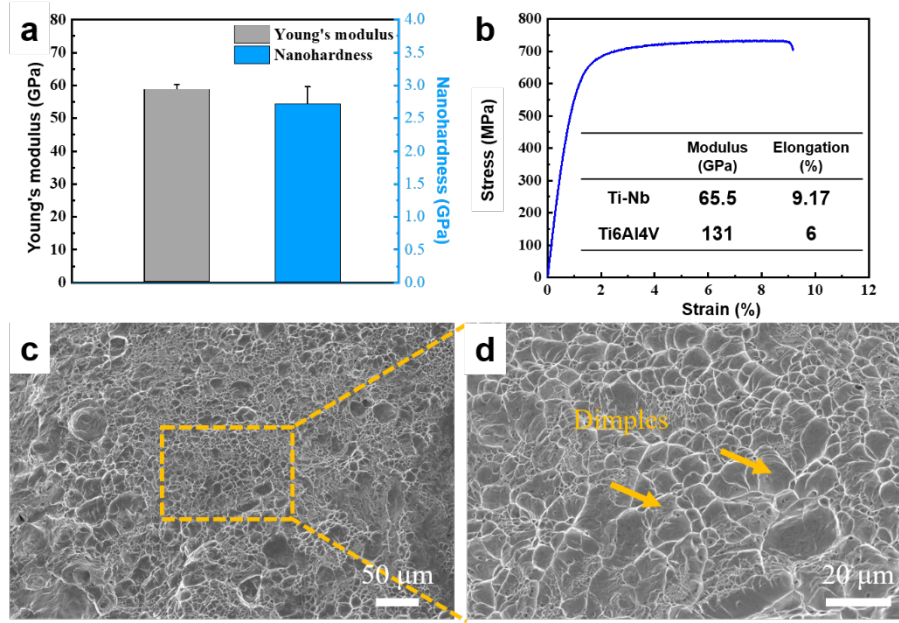


Fig. 5. Mechanical properties of Ti-Nb alloy non-porous meshes. **(a)** elastic modulus and nano-hardness from nano-indentation analysis, **(b)** Tensile stress-strain response and **(c-d)** The representative fracture surface after tensile tests.

3.3 Mechanisms of the EPD process

Fig. 6a-b exhibit the physical properties of the coatings. The chitosan (CS), gelatin (G) and doxycycline (Dox) were positively charged with a zeta potential of $\sim +18.4$ mV, $+3.66$ mV and $+11.97$ mV in aqueous solution, respectively. The CSG, CSGDox1 and CSGDox10 were positively charged with a zeta potential of $\sim +18.53$ mV, $+11.23$ mV and $+5.67$ mV, respectively (Fig. 6a). The equivalent diameters of CS, G and Dox particles ranged from 1400 to 6600 nm, 100 to 250 nm and 1000 to 2000 nm, respectively (Fig. 6b). When CSG was mixed with two concentrations of Dox, the size increased to an average diameter of about 1.13×10^5 and 1.54×10^5 nm.

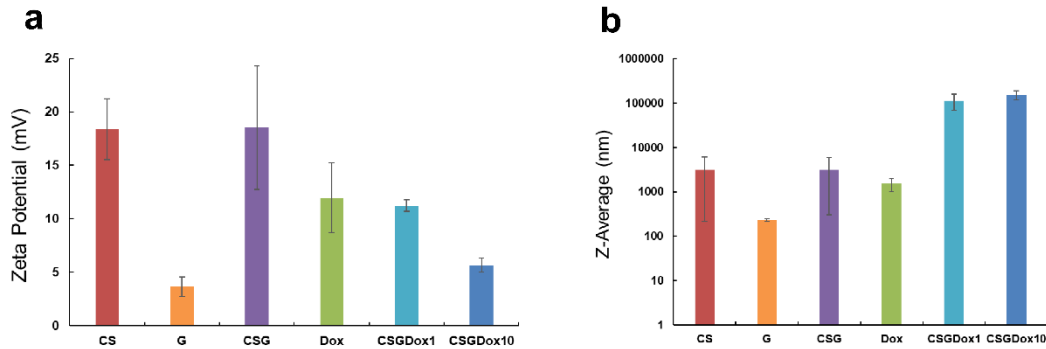


Fig. 6. Physical properties of solute in EPD solutions. **(a)** The zeta potential and **(b)**

particle size analysis of coatings EPD solutions.

The FT-IR spectra of CSG, Dox, CSGDox1 and CSGDox10 are shown in Fig. 7. Since the characteristic region of the CS, G and Dox occurred between 1000 cm^{-1} and 1800 cm^{-1} , only this region was interpreted in detail. The characteristic peaks of C–O–C stretching structure at 1028 cm^{-1} , and C–O–C antisymmetric stretching structure at 1150 cm^{-1} were visible in the CSG spectrum, which was related with CS [9]. The distinctive peaks at 1643 cm^{-1} and 1552 cm^{-1} due to amide I (C=O stretching) and amide II (C–N stretching) could be attributed to G [22]. The spectrum of Dox displayed the peaks of amide bond structure in ring A at 1662 cm^{-1} . It also showed the distinctive peaks of carbonyl groups in rings A and C at 1610 cm^{-1} , 1576 cm^{-1} , and 1558 cm^{-1} , and the C=C skeleton vibration at 1460 cm^{-1} .

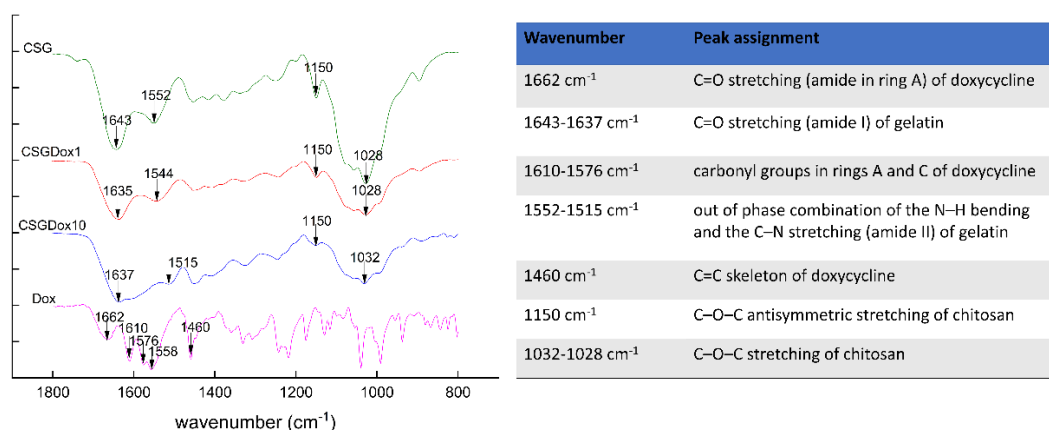


Fig. 7. FT-IR spectroscopy detection of the coatings and the peak assignments.

3.4 *In vitro* antibacterial activity

The antibacterial efficacy was investigated using inhibition zone testing and SEM. The tests were maintained for at least 7 days, a critical time point for the healing of oral mucosa [4]. Titanium substrates and CSG coatings did not exhibit any inhibition zone against *S. aureus* (Fig. 8a-b). The contact inhibition properties of CSGDox1 and CSGDox10 coatings can be measured by the obvious inhibition zones around the samples after 24h incubation due to the release of Dox (Fig. 8c-d). The diameters of the inhibition zone for CSGDox1 and CSGDox10 coatings were measured about 30.5 mm and 36.7 mm respectively, and the inhibition zone could be maintained for at least 7 days (Fig. 8e). As demonstrated, the EPD of CSGDox1 and CSGDox10 coatings onto titanium substrate produced an efficient antimicrobial effect.

SEM images also provided further confirmation of the significant antimicrobial effects (Fig. 8f-i). After 24 h, the significant growth of the layered *S. aureus* could be observed. *S. aureus* attached and aggregated on the surfaces of the titanium substrates and CSG coatings (Fig. 8f and g). However, almost no adherent microbial cells were observed on the surface of the Dox-loaded coatings, suggesting a powerful control against the adherence and colonization of bacteria.

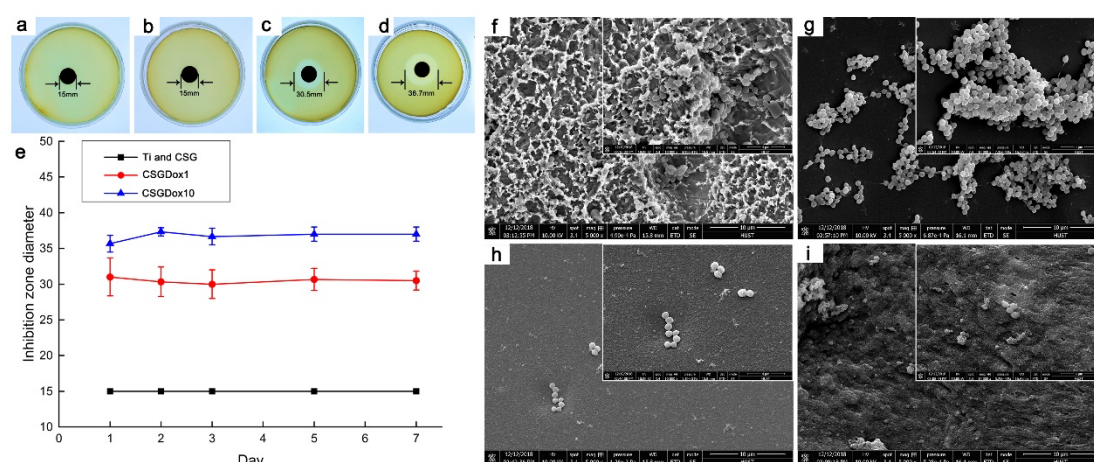


Fig. 8. The inhibition zone diameters of *S. aureus* on the titanium substrates (a) Control group, (b) CSG coating, (c) CSGDox1 coating, (d) CSGDox10 coating, and (e) Inhibition zone diameter following 1, 2, 3, 5 and 7 days. SEM images of *S. aureus* colonization (24 h) on the inhibition zone of (f) Control group, (g) CSG coating, (h) CSGDox1 coating and (i) CSGDox10 coating.

3.5 Initial cell response

The biocompatibility of the CSG, CSGDox1 and CSGDox10 coatings were evaluated through the culture of osteoblasts. After 72h of culture, a close contact with osteoblasts was achieved for all three kinds of coatings (Fig. 9). These cells presented numerous lamellipodia and filopodia, anchoring the cells to the sample surfaces. The images revealed the actin cytoskeleton, which provides a structural framework and participates in cell migration. These actin-rich structures are termed as tunneling nanotubes, which can mediate the intercellular transfer of organelles, plasma membrane components, and cytoplasmic molecules. Notably, MC3T3-E1 cells treated in CSG and CSGDox1 surfaces spread more widely than that on the CSGDox10 surfaces, extended more pseudopodia, anchored in the coatings, and appeared to be star-like morphology. On the contrary, with the increase of doxycycline, a spindle-like morphology of osteoblasts was exhibited on CSGDox10 which demonstrated the worst cell-adhesion

ability, the cells extended fewer pseudopodia, and were sparser and smaller than that on CSG and CSGDox1, which may be attributed to the cytotoxicity of Dox. Therefore, considering the cytotoxicity and antimicrobial activity *in vitro*, we decided to choose the concentration of 1mg /ml Dox for further experiments on the coatings.

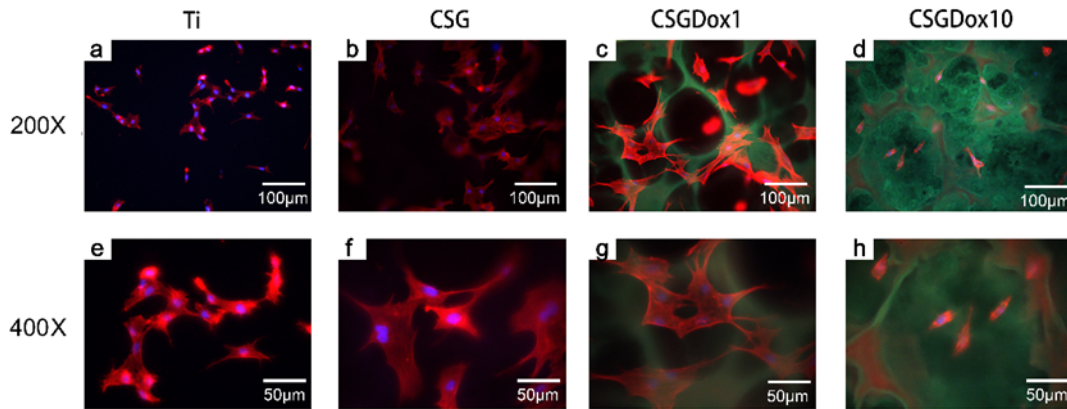


Fig. 9. Confocal immunofluorescence staining of osteoblast nuclei with DAPI and F-actins with rhodamine phalloidin on CSG, CSGDox1, CSGDox10 coatings.

3.6 Morphologies of the CSGDox1 coating on the porous Ti-Nb alloy meshes

Fig. 10a-c shows the morphologies of CSGDox1 coating on the three Ti-Nb alloy meshes (T1000, H1000 and R1000). After lyophilization, it could be observed that CSGDox1 coatings were uniformly deposited onto both sides of the Ti-Nb alloy meshes after EPD. The sponge-like coatings showed a similar thickness with effective coverage of the pore structures (Fig. 10a-c). The coatings presented a faint yellow color due to the crosslinking with Dox.

Fig. 10d-f presents the SEM images showing the surface morphologies of the coatings on the meshes. A homogeneous and porous structure was observed, which may be resulted by the desiccation and collapse of bubble formation during the EPD process. The pore sizes ranged from 200–300 µm; an optimal diameter for bone tissue in-growth [23, 24]. The coating effectively closed the Ti-Nb mesh's pores, reducing the likelihood of fibroblast infiltration, which is essential during the GBR process.

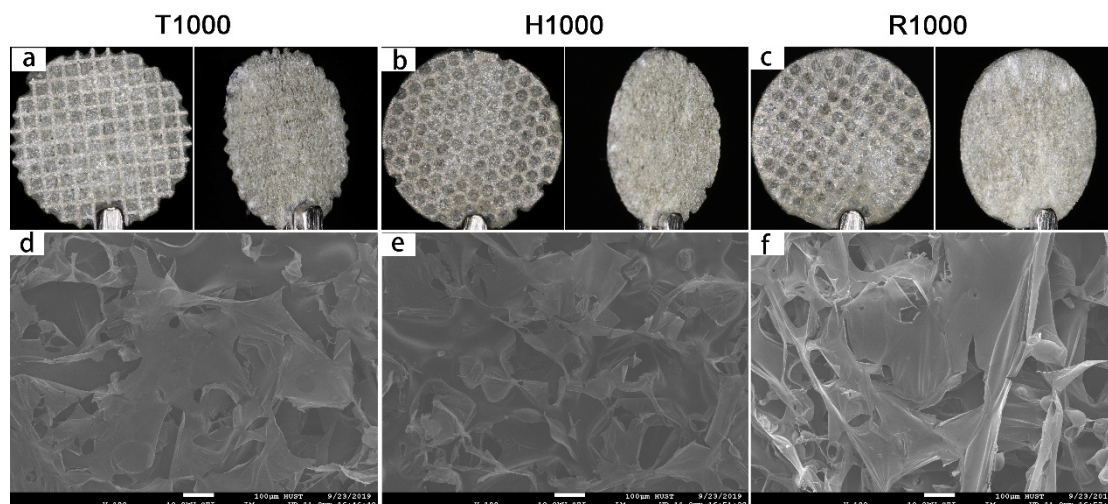


Fig. 10. Macroscopic images of CSGDox1 coating on three types of Ti-Nb meshes: **(a)** T1000, **(b)** H1000 and **(c)** R1000. The SEM images of CSGDox1 coating on **(d)** T1000, **(e)** H1000 and **(f)** R1000.

3.7 Inhibition of fibroblasts infiltration

Infiltration of fibroblasts into the bone defect area could be detrimental to osteogenesis during the early stages of GBR. CSGDox1 coatings were tested to block the fibroblasts migration. The fibroblasts were seeded and cultivated on the upper surfaces of each porous Ti-Nb mesh using a relevant *in vitro* model. The cell blocking capacity of CSGDox1 was presented in Fig. 11. After 72h culture, immunofluorescence images revealed that a large number of fibroblasts could be observed on the upper surfaces of each porous Ti-Nb alloy substrates (Fig. 11a-c). Conversely, no cells were observed on the lower surfaces, and none were observed at the bottom of the 24-well plate (Fig. 11d-f). This indicated that the CSGDox1 coating was capable to block the infiltration of fibroblasts through controlling the size of the pores.

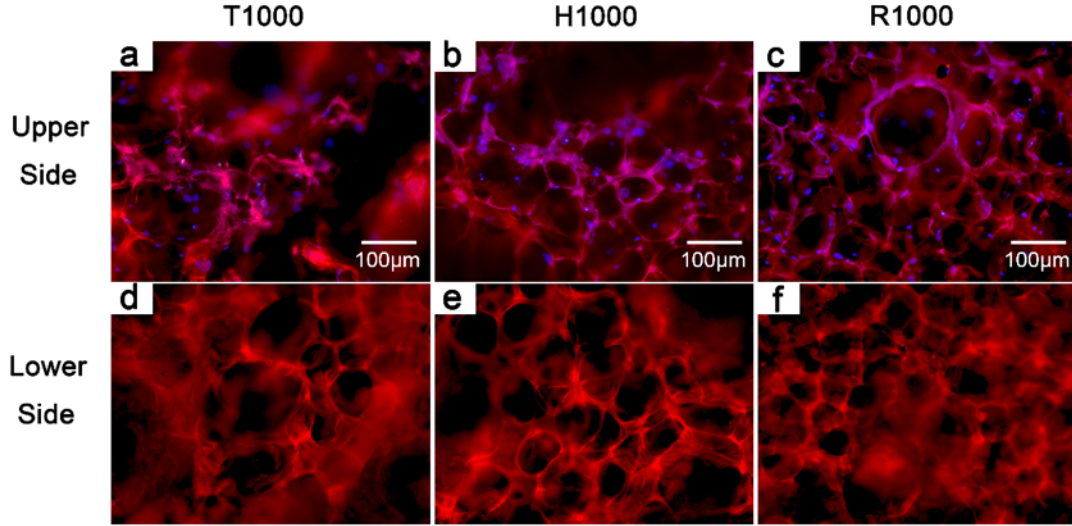


Fig. 11. The confocal immunofluorescence staining of nuclei with DAPI and F-actins with rhodamine phalloidin in fibroblasts from upper (**a-c**) and lower (**d-f**) surface of T1000, H1000 and R1000, respectively.

3.8 Diffusion of proteins

Fig. 12 shows the nutrient transfer properties of CSGDox1 coatings on the porous Ti-Nb alloy meshes. The protein permeability of the coatings was investigated using 1 mL of 70 mg/mL BSA solution as a model protein since most nutrients have a much smaller size than albumin (Mw 69,000) [25], and the concentration of BSA (70 mg/mL) is similar to that of total plasma protein. Only 1 mL of BSA solution was applied to minimize the effect of fluid pressure and gravity on the effective permeability of protein. The effective permeability of T1000, H1000 and R1000 meshes were calculated as $256.92 \pm 9.82 \text{ mL}/(\text{m}^2 \cdot \text{s})$, $195.71 \pm 11.91 \text{ mL}/(\text{m}^2 \cdot \text{s})$ and $183.53 \pm 15.06 \text{ mL}/(\text{m}^2 \cdot \text{s})$, respectively (Fig. 12). There is a statistically significance between T1000-H1000 and T1000-R1000 ($P < 0.01$), but none was found between H1000 and R1000. Compared with H1000 and R1000, T1000 had the highest permeability due to its largest projected area of the pore, which may lead to a timelier effect for providing essential nutrients for bone regeneration.

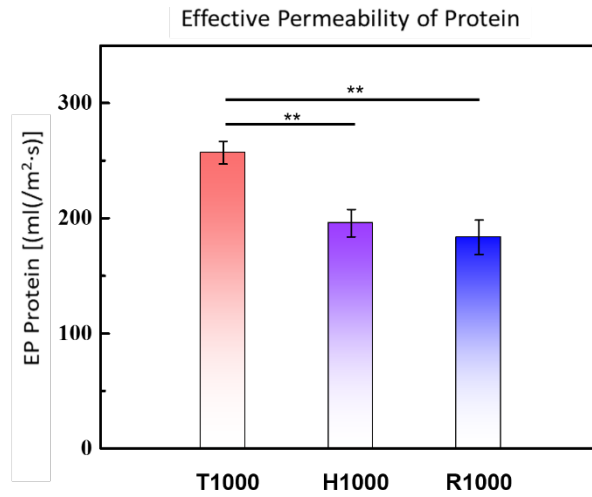


Fig. 12. The effective permeability of protein of CSGDox1 coatings on the Ti-Nb alloy meshes, $**P<0.01$).

4. Discussion

In this study, novel semi-permeable CSGDox coatings were constructed on the 3D-printed Ti-Nb meshes through the EPD process, which is an admirable method for the function design of the porous metallic structure. The CSGDox coatings possessed sustained antibacterial efficacy within 7 days and favorable cytocompatibility. Moreover, the coatings could simultaneously allow nutrient transfer and block the infiltration of fibroblasts by controlling the size of the pores.

4.1 3D-printed Ti-Nb alloy meshes

The efficacy of titanium implants used for GBR is limited by the anatomical mismatch and potential displacement during implantation. Additive manufacturing may overcome these limitations by printing meshes that conform to the dimensions of the defect site. The high reliability of processing intricate mesh structures in this work demonstrated the freedom of fabrication capacity of the SLM technique. Moreover, the uniform element distribution proved that SLM enhanced Nb element distribution and aided diffusion between Ti and Nb, thus avoiding the apparent elemental segregation in conventionally cast samples [26]. The uniform distribution of elements resulted in less micro-segregation, lower elastic modulus and higher corrosion resistance [27].

In addition, the elastic modulus of Ti-Nb alloy was lower than that of Ti6Al4V (131 GPa) and commercially pure Ti (137 GPa) [28]. Due to the stabilization of the β -phase by Nb addition, the substantial decrease in rigidity of the Ti-Nb alloy would reduce the modulus mismatch between the implant and adjacent bone tissue, lessening the effects

of stress-shielding.

4.2 Physicochemical characterization of the coatings

The formation of the CSGDox coatings was assessed by zeta potential and particle size analysis. Chitosan is a linear polysaccharide, which has primary amino groups with a pK-value of ~ 6.3 . It was positively charged with a zeta potential of about +18.4 mV in acid solution at pH 4. When the gelatin colloid was blended into chitosan solution, the zeta potential of the CS/G remained constant. With the addition of Dox into CSG, the zeta potential decreased from +18.53 to +5.67 mV, which was agreed with Xu et al. [29]. Therefore, it indicated that the polyelectrolyte complex might be formed by the electrostatic interaction between the cationic amino group of chitosan and the hydroxy groups of Dox [16, 30]. Moreover, the addition of Dox led to the increase of particle size. The increase in particle size of CSGDox1 and CSGDox10 also indicated that electrostatic adsorption of CSG onto Dox was formed, and then co-deposited to the titanium surface on Cathode driven by the electric field [31, 32].

The FT-IR showed that both the absorption peaks of the saccharine and amide appeared in the spectrum of CSG composite coatings. The absorption of Dox is often obscured by the stronger amide I and II absorption. Therefore, the addition of Dox led to a shift of the absorption peaks of amide II (-NH_2 stretching) from 1552 cm^{-1} to 1515 cm^{-1} . Furthermore, it may be induced by the secondary structure of G which is formed through the hydrogen bonding of the amide with Dox [33]. In addition, the characteristic peaks of Dox at 1610 cm^{-1} , 1576 cm^{-1} , and 1558 cm^{-1} were no longer observed in the spectra of CSGDox1 and CSGDox10. The results are similar to the experiment of Walter MS and Zehtabi F et.al [17, 33]. The shifting of the 1552 cm^{-1} band and the disappearance of bands indicated that there are certain chemical reactions between Dox and CSG, which inhibited the motion of vibration [34]. The data was consistent with the results of the zeta analysis.

4.3 Antimicrobial effect

Granulated tissue formation and the lack of adequate bone callus formation are mainly induced by the exposure of the graft material to the oral environment and consequent infection [35]. Dox has been clinically applied as a broad-spectrum antibiotic in orthopedic surgery by inhibiting the biosynthesis of bacterial protein with

ribosomes [36, 37]. The activity of CSGDox coating against bacterial biofilms was determined by measuring the zone of inhibition (Fig. 8a-e). *In vitro* infection test suggested that almost no bacteria was survived on the CSGDox coatings. The results were agreed with the work of Moghaddam et al., which reported the inability of the bacteria to grow in Dox-loaded drugs though targeting the population of intracellular bacteria [38]. Additionally, the SEM images indicated that the coatings could produce not only antibacterial but also anti-adherent effects, leading to the eradication of microorganisms. The biofilm controlling function of the CSGDox coating was attributed to the antimicrobial activities of the Dox. Importantly, the release of antimicrobial effectivity could be maintained with 7 days. Feng et al. also proposed that Dox packed in the drug-loaded system could be released continuously with better efficacy [39]. The antibacterial effect could help osteoblasts to proliferate on the implant surface and prevent the colonization of bacteria at an early stage, thereby achieving a successful outcome.

4.4 Biocompatibility

To evaluate the initial osteoblastic response in contact with the coatings, osteoblast-like cells (MC3T3) were seeded and cultivated on the titanium substrate, CSG coatings and Dox loaded coatings. The osteoblasts on the CSGDox1 coatings exhibited better proliferation and spreading with elongated filopodia than that on the CSGDox1 coatings. The response suggested that the higher addition of Dox was detrimental to the cytocompatibility of the coatings. Ma et al. observed higher cytotoxicity of CSG tetracycline (Tc)10 coatings than Tc1 coatings [40]. Other kinds of antibiotics, such as chlorhexidine (CHX) and minocycline (MINO), also showed a cytotoxic effect on osteoblast proliferation *in vitro* at a high concentration [41]. Sagar et al. elucidated that Dox could induce apoptosis through mitochondrial-mediated pathways in different tissue cells and Dox may be cytotoxic *in vitro* [28]. The concentration of antibiotics may be an important factor affecting its cytotoxicity. Rok et al. [29] stated that Dox disturbed the homeostasis of melanoma cells by lowering the intracellular level of reduced thiols, changing the cell cycle profile, triggering the DNA fragmentation and inducing the externalization phosphatidylserine which is a well-known hallmark of apoptosis [42].

4.5 Bioadaptive function and outlook

In addition to favorable biocompatibility and antibiotic ability, a GBR membrane should be capable to prevent excessive penetration of oral soft tissue into the bone defect from one side but allow neovascularization and bone formation from the connective tissue side of the membrane. The combination of three-dimensional meshes and CSGDox1 coating was capable to block the infiltration of fibroblasts and allow nutrient transfer through controlling the size of the pores, which is smaller than the size of fibroblast and larger than that of protein. Moreover, the permeation of protein could be affected by the surface wettability and hygroscopicity of the membrane at the similar pore size [43]. The favorable protein permeates quality is predictable due to the well hydrophilicity and wettability of CSGDox1 coating [44]. As a result, the blood can permeate through the CSGDox1 coated porous Ti-Nb alloy meshes quickly to the bone defect area, which leads to a better effect of providing bone regeneration essential nutrients timely. It was expected that the porous coating can effectively prevent fibrous tissue infiltration but permeate nutrients, while the micro-pore side can improve adhesion with surrounding bone tissue, resulting in enhanced bone regeneration.

Although we studied the *in vitro* cellular response of coatings, the *in vivo* results of animals could be more valuable and closely simulate the clinical situation. Therefore, *in vivo* evaluation of antibacterial capacity and cell penetration is required for further applications. Moreover, the final goal of developing functional coatings is to be combined with biodegradable meshes for one-step treatment of bone defects. Considering the degradability, more research works would be systematically conducted on the dynamic balancing of the stability of coatings and the degradation of meshes.

5. Conclusions

In this study, Ti-Nb alloy meshes with various shapes were fabricated by SLM and used as substrates for novel surface coatings. Doxycycline-loaded chitosan/gelatin films were deposited on each mesh by EPD to provide antibiotic properties and physical barriers to prevent gingival tissue ingrowth. High strength and low modulus were achieved in the Ti-Nb alloy block samples. The CSGDox1 coating exhibited favorable biocompatibility, and the ability to inhibit fibroblast infiltration to prevent the ingrowth of soft tissues while allowing the transfer of essential nutrients. The incorporation of doxycycline enhanced the antimicrobial activity of coatings, which could benefit the success rate and prognosis of bone regeneration. This study has developed novel semi-

permeable coatings on 3D-printed Ti-Nb alloy meshes that may improve the success and outcome of GBR and offers a new strategy for alveolar bone defect regeneration.

Acknowledgment

The research was supported by the National Natural Science Foundation of China (51775207), the Academic frontier youth team at Huazhong University of Science and Technology, the Science and Technology Major Project of Guangdong Province (2017B090911007) and Application Fundamentals frontier Major Project of Wuhan (2018010401011281). The authors acknowledge the State Key Laboratory of Materials Processing and Die & Mould Technology and the Analysis and Testing Center of Huazhong University of Science and Technology for technical assistance.

References

- [1] Bottino MC, Thomas V, Schmidt G, Vohra YK, Chu TM, Kowolik MJ, et al. Recent advances in the development of GTR/GBR membranes for periodontal regeneration--a materials perspective. *Dent Mater*. 2012;28:703-21.
- [2] Kloss FR, Offermanns V, Kloss-Brandstätter A. Comparison of allogeneic and autogenous bone grafts for augmentation of alveolar ridge defects—A 12-month retrospective radiographic evaluation. *Clinical Oral Implants Research*. 2018;29:1163-75.
- [3] Miyamoto I, Funaki K, Yamauchi K, Kodama T, Takahashi T. Alveolar Ridge Reconstruction with Titanium Mesh and Autogenous Particulate Bone Graft: Computed Tomography-Based Evaluations of Augmented Bone Quality and Quantity. *Clinical Implant Dentistry and Related Research*. 2012;14:304-11.
- [4] Wang HL, Boyapati L. "PASS" principles for predictable bone regeneration. *Implant Dent*. 2006;15:8-17.
- [5] Zhang T, Zhang T, Cai X. The application of a newly designed L-shaped titanium mesh for GBR with simultaneous implant placement in the esthetic zone: A retrospective case series study. *Clinical Implant Dentistry and Related Research*. 2019;21:862-72.
- [6] Her S, Kang T, Fien MJ. Titanium Mesh as an Alternative to a Membrane for Ridge Augmentation. *Journal of Oral and Maxillofacial Surgery*. 2012;70:803-10.
- [7] Zhao D, Huang Y, Ao Y, Han C, Wang Q, Li Y, et al. Effect of pore geometry on the fatigue properties and cell affinity of porous titanium scaffolds fabricated by selective laser melting. *Journal of the Mechanical Behavior of Biomedical Materials*. 2018;88:478-87.
- [8] Zhang S, Cheng X, Yao Y, Wei Y, Han C, Shi Y, et al. Porous niobium coatings fabricated with selective laser melting on titanium substrates: Preparation, characterization, and cell behavior. *Materials Science and Engineering: C*. 2015;53:50-9.
- [9] Zhang Z, Jiang T, Ma K, Cai X, Zhou Y, Wang Y. Low temperature electrophoretic deposition of porous chitosan/silk fibroin composite coating for titanium biofunctionalization. *Journal of Materials Chemistry*. 2011;21:7705-13.
- [10] Qasim SB, Najeeb S, Delaine-Smith RM, Rawlinson A, Ur Rehman I. Potential of electrospun

chitosan fibers as a surface layer in functionally graded GTR membrane for periodontal regeneration. *Dent Mater*. 2017;33:71-83.

[11] Li D, Zhao L, Cong M, Liu L, Yan G, Li Z, et al. Injectable thermosensitive chitosan/gelatin-based hydrogel carried erythropoietin to effectively enhance maxillary sinus floor augmentation in vivo. *Dental Materials*. 2020;36:e229-e40.

[12] Han C, Yao Y, Cheng X, Luo J, Luo P, Wang Q, et al. Electrophoretic Deposition of Gentamicin-Loaded Silk Fibroin Coatings on 3D-Printed Porous Cobalt-Chromium-Molybdenum Bone Substitutes to Prevent Orthopedic Implant Infections. *Biomacromolecules*. 2017;18:3776-87.

[13] Zhang Z, Cheng X, Yao Y, Luo J, Tang Q, Wu H, et al. Electrophoretic deposition of chitosan/gelatin coatings with controlled porous surface topography to enhance initial osteoblast adhesive responses. *Journal of Materials Chemistry B*. 2016;4:7584-95.

[14] Rafael Poveda Roda, José Vicente Bagán, José María Sanchis Bielsa, Pastor EC. Antibiotic use in dental practice a review. *Med Oral Patol Oral Cir Bucal*. 2007;12:E186-92.

[15] Kuhn KD, Renz N, Trampuz A. [Local antibiotic therapy]. *Unfallchirurg*. 2017;120:561-72.

[16] Zhang Z, Qu Y, Li X, Zhang S, Wei Q, Shi Y, et al. Electrophoretic deposition of tetracycline modified silk fibroin coatings for functionalization of titanium surfaces. *Applied Surface Science*. 2014;303:255-62.

[17] Walter MS, Frank MJ, Satue M, Monjo M, Ronold HJ, Lyngstadaas SP, et al. Bioactive implant surface with electrochemically bound doxycycline promotes bone formation markers in vitro and in vivo. *Dent Mater*. 2014;30:200-14.

[18] Zhang P, Ding L, Kasugai S. Effect of doxycycline doped bone substitute on vertical bone augmentation on rat calvaria. *Dent Mater J*. 2019;38:211-7.

[19] Silva AC, Oliveira MR, Amaral LF, Ferreira S, Garcia IR, Jr., Mariano RC. Effect of Doxycycline in Gel Form on Bone Regeneration: Histomorphometric and Tomographic Study in Rat Calvaria. *J Periodontol*. 2016;87:74-82.

[20] Liang H, Zhao D, Feng X, Ma L, Deng X, Han C, et al. 3D-printed porous titanium scaffolds incorporating niobium for high bone regeneration capacity. *Materials & Design*. 2020;194:108890.

[21] Sing SL, Yeong WY, Wiria FE. Selective laser melting of titanium alloy with 50 wt% tantalum: Microstructure and mechanical properties. *Journal of Alloys and Compounds*. 2016;660:461-70.

[22] Jiang T, Zhang Z, Zhou Y, Liu Y, Wang Z, Tong H, et al. Surface functionalization of titanium with chitosan/gelatin via electrophoretic deposition: characterization and cell behavior. *Biomacromolecules*. 2010;11:1254-60.

[23] Kane R, Ma PX. Mimicking the nanostructure of bone matrix to regenerate bone. *Mater Today (Kidlington)*. 2013;16:418-23.

[24] Bose S, Roy M, Bandyopadhyay A. Recent advances in bone tissue engineering scaffolds. *Trends Biotechnol*. 2012;30:546-54.

[25] Nieman DC, Butterworth DE, Nieman CN. *Nutrition*. 1990.

[26] Daudt NF, Hackemueller FJ, Bram MJML. Manufacturing of Ti-10Nb based metal sheets by tape casting. 2018;237:161-4.

[27] Zhao D, Han C, Li J, Liu J, Wei Q. In situ fabrication of a titanium-niobium alloy with tailored microstructures, enhanced mechanical properties and biocompatibility by using selective laser melting. *Materials Science and Engineering: C*. 2020;111:110784.

[28] Han C, Wang Q, Song B, Li W, Wei Q, Wen S, et al. Microstructure and property evolutions of titanium/nano-hydroxyapatite composites in-situ prepared by selective laser melting. 2017;71:85.

- [29] Xu S, Zhou Q, Jiang Z, Wang Y, Yang K, Qiu X, et al. The effect of doxycycline-containing chitosan/carboxymethyl chitosan nanoparticles on NLRP3 inflammasome in periodontal disease. *Carbohydrate Polymers*. 2020;237:116163.
- [30] Song J, Chen Q, Zhang Y, Diba M, Kolwijck E, Shao J, et al. Electrophoretic Deposition of Chitosan Coatings Modified with Gelatin Nanospheres To Tune the Release of Antibiotics. *ACS Applied Materials & Interfaces*. 2016;8:13785-92.
- [31] Boccaccini AR, Keim S, Ma R, Li Y, Zhitomirsky I. Electrophoretic deposition of biomaterials. *Journal of The Royal Society Interface*. 2010;7:S581-S613.
- [32] Seuss S, Boccaccini AR. Electrophoretic Deposition of Biological Macromolecules, Drugs, And Cells. *Biomacromolecules*. 2013;14:3355-69.
- [33] Zehtabi F, Ispas-Szabo P, Djerir D, Sivakumaran L, Annabi B, Soulez G, et al. Chitosan-doxycycline hydrogel: An MMP inhibitor/sclerosing embolizing agent as a new approach to endoleak prevention and treatment after endovascular aneurysm repair. *Acta Biomater*. 2017;64:94-105.
- [34] Tamimi F, Torres J, Bettini R, Ruggera F, Rueda C, López-Ponce M, et al. Doxycycline sustained release from brushite cements for the treatment of periodontal diseases. *J Biomed Mater Res A*. 2008;85:707-14.
- [35] Machtei EE. The Effect of Membrane Exposure on the Outcome of Regenerative Procedures in Humans: A Meta-Analysis. *J Periodontol*. 2001;72:5.
- [36] Shanmuganathan S, Shanumugasundaram N, Adhirajan N, Ramyaa Lakshmi TS, Babu M. Preparation and characterization of chitosan microspheres for doxycycline delivery. *Carbohydrate Polymers*. 2008;73:201-11.
- [37] Hong W, Zeng J, Xie J. Antibiotic drugs targeting bacterial RNAs. *Acta Pharmaceutica Sinica B*. 2014;4:258-65.
- [38] Hafezi Moghaddam R, Dadfarnia S, Shabani AMH, Amraei R, Hafezi Moghaddam Z. Doxycycline drug delivery using hydrogels of O-carboxymethyl chitosan conjugated with caffeic acid and its composite with polyacrylamide synthesized by electron beam irradiation. *International Journal of Biological Macromolecules*. 2020;154:962-73.
- [39] Feng C, Wang Z, Jiang C, Kong M, Zhou X, Li Y, et al. Chitosan/o-carboxymethyl chitosan nanoparticles for efficient and safe oral anticancer drug delivery: In vitro and in vivo evaluation. *International Journal of Pharmaceutics*. 2013;457:158-67.
- [40] Ma K, Cai X, Zhou Y, Wang Y, Jiang T. In Vitro and In Vivo Evaluation of Tetracycline Loaded Chitosan-Gelatin Nanosphere Coatings for Titanium Surface Functionalization. *Macromol Biosci*. 2017;17.
- [41] Soriano-Souza C, Valiense H, Mavropoulos E, Martinez-Zelaya V, Costa AM, Alves AT, et al. Doxycycline containing hydroxyapatite ceramic microspheres as a bone-targeting drug delivery system. *J Biomed Mater Res B Appl Biomater*. 2020;108:1351-62.
- [42] Rok J, Karkoszka M, Rzepka Z, Respondek M, Banach K, Beberok A, et al. Cytotoxic and proapoptotic effect of doxycycline - An in vitro study on the human skin melanoma cells. *Toxicol In Vitro*. 2020;65:104790.
- [43] Oh SH, Kim JH, Kim JM, Lee JH. Asymmetrically porous PLGA/Pluronic F127 membrane for effective guided bone regeneration. *J Biomater Sci Polym Ed*. 2006;17:1375-87.
- [44] Cho WJ, Kim JH, Oh SH, Nam HH, Kim JM, Lee JH. Hydrophilized polycaprolactone nanofiber mesh-embedded poly(glycolic-co-lactic acid) membrane for effective guided bone regeneration.

J Biomed Mater Res A. 2009;91:400-7.